Fokas Based Dirichlet-to-Neumann Operators for Accurate Signal Integrity Assessment of Interconnects

Martijn Huynen, Dries Bosman, Daniël De Zutter, and Dries Vande Ginste

Quest Lab, IDlab, Ghent University/imec, Belgium

***Abstract*—In this contribution, we present a new approach to fully characterize interconnects composed out of arbitrary polygonal cross-sections and containing piecewise homogeneous material parameters. The complex per-unit-of-length inductance and capacitance matrices are obtained through the application of pertinent Dirichlet-to-Neumann operators, which are computed by means of an extended Fokas method, that are integrated in a boundary integral equation approach. As the complete RLGC-data of the structures under study is computed, we are able to assess relevant properties such as signal attenuation and cross-talk while the support for polygonal shapes allows for the inclusion of manufacturing effects such as etching.**

***Index Terms*—Dirichlet-to-Neumann operator, Fokas method, interconnect modeling, per-unit-of-length parameters.**

I. Introduction

The continuous drive for integration of electronic-based capabilities into every single aspect of our information-centered society has been advancing at breakneck speed for the past few decades. The resulting miniaturization and complexity of the integrated interconnect structures operating at ever higher frequencies has led to an increased influence of their losses and dispersion on the signal integrity of the signals they carry. However, as the cross-section generally still remains smaller than the smallest wavelength, a quasi-transverse magnetic (TM) electromagnetic analysis that computes the frequency-dependent per unit-of-length (p.u.l.) RLGC transmission line parameters remains an indispensable tool to accurately determine the behavior of critical lines. Moreover, as we require a description of the interconnect from DC up to tens of GHz, the simulation method needs to account for all electromagnetic phenomena in the employed materials, such as the slow-wave effect, skin effect, current crowding and conductor losses, that cover various, drastically different operation regimes.

In the context of boundary integral equation (BIE) approaches, the difficulty in accurately capturing the exponential field distributions due to the current crowding, surfaces in the correct numerical integration of the Green's function in the conductive media, which requires special care [1]. Hence, alternative approaches have been developed that mitigate the issue by replacing the conductive medium by the background material and then applying the appropriate boundary conditions, ranging from approximate, local surface impedances [2] to exact, global relations such as the differential surface admittance (DSA) operator [3]. In recent work [4], we proposed a novel technique to compute this operator, which no longer relied on the eigenmodes of the shapes such as circles [5] or triangles [6], but instead utilizes the Fokas method or unified transform [7] to find the DSA matrix for any convex polygons and allows for combined magnetic and dielectric contrast.

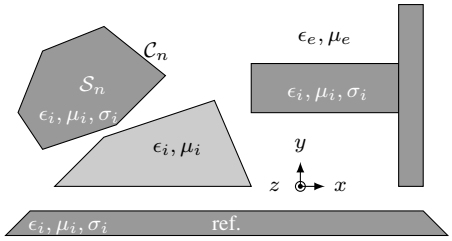

Figure 1. General representation of a multiconductor transmission line's cross-section including dielectrics and signal and reference conductors.

In this contribution, we extend the work in [4] to compute not only the complex p.u.l. inductance but the complex p.u.l. capacitance as well. To compute this missing half of the RLGC-parameters, we modify the Fokas-based computation of the DSA operator to construct a dedicated Dirichlet-to-Neumann (DtN) operator for the differential equation governing the capacitance problem. Combined, these two calculation methods enable us to fully assess signal integrity (SI) performance of non-ideal interconnects, including a strongly developed skin effect. Moreover, we show that magnetic materials, which are nowadays emerging in more and more on-chip applications can also be included in our method.

II. Formulation of the method

Assume a quasi-TM, time-harmonic configuration with an $e^{j\omega t}$ dependency. Furthermore, consider the general representation of a multiconductor transmission line's cross-section shown in Fig. 1. The geometry consists of arbitrary polygonal elements $\mathcal{S}_n$ embedded in a homogeneous background medium with permittivity ϵ_e and permeability μ_e. Each polygonal element represents a signal conductor, reference conductor or (lossy) dielectric, all characterized by a set of material parameters $(\epsilon_i, \mu_i, \sigma_i)$.

In [4], the procedure to compute the p.u.l. $\overline{\overline{R}}$ and $\overline{\overline{L}}$ matrix is outlined in full detail and for the sake of brevity it will not be repeated here. Instead, we turn our attention directly to the computation of the p.u.l. capacitance $\overline{\overline{C}}$ and p.u.l. conductance $\overline{\overline{G}}$ matrices by solving the relevant complex capacitance problem. Thereto, we extend the approach developed for

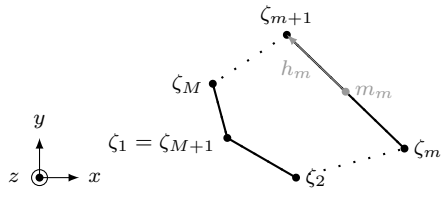

Figure 2. Geometry of an arbitrary polygonal element, illustrating the necessary definitions for the Fokas-based derivation of the DtN operator.

rectangular cross-sections in [8] to support polygonal shapes by including a Fokas-based global relation.

We start by replacing all dielectric objects by the background medium through introduction of the pertinent contrast surface charge density defined as $\rho_{\text{eq}} = -(\epsilon - \epsilon_e)e_n$, with e_n the outward pointing normal electric field. Following the approach detailed in [8], we approximate e_n by $-\partial_n\phi$ and by introducing the DtN operator $\mathcal{D}$, which couples ϕ and its normal derivative on the boundary of the replaced medium, we rewrite the previously established relation as

$$\rho_{\text{eq}} = (\epsilon - \epsilon_e)\mathcal{D}\phi = \mathcal{D}'\phi, \tag{1}$$

where we will determine $\mathcal{D}$ by means of a Fokas method as detailed further on in this section. These charge densities in turn induce a potential ϕ, given by

$$\phi(\mathbf{r}) = -\frac{1}{\epsilon_0}\oint_{\mathcal{C}} \rho_{\text{eq}}(\mathbf{r}')\, G(\mathbf{r},\mathbf{r}')\, \mathrm{d}c(\mathbf{r}'), \tag{2}$$

with G the (static) Green's function of the governing Laplace equation $\nabla^2\phi = 0$.

Discretizing (2) for both dielectrics (subindex d) and conductors (subindex c) and (1) for the dielectric elements by means of a Galerkin approach with pulse basis functions, results in the following matrix equation

$$\begin{pmatrix} \overline{\overline{A}}_{\text{cc}} & \overline{\overline{A}}_{\text{cd}}\overline{\overline{\Gamma}}_{\text{dd}}^{-1}\overline{\overline{D}}' \\ \overline{\overline{A}}_{\text{dc}} & \overline{\overline{A}}_{\text{dd}}\overline{\overline{\Gamma}}_{\text{dd}}^{-1}\overline{\overline{D}}' - \overline{\overline{\Gamma}}_{\text{dd}} \end{pmatrix} \begin{pmatrix} \boldsymbol{\rho}_{\text{c}} \\ \boldsymbol{\phi}_{\text{d}} \end{pmatrix} = \begin{pmatrix} \overline{\overline{\Gamma}}_{\text{cc}}\boldsymbol{\phi}_{\text{c}} \\ \mathbf{0} \end{pmatrix}, \tag{3}$$

with the (sub)matrices $\overline{\overline{A}}_{\text{xx}}$ the pertinent parts of the discretized integral equation (2), $\overline{\overline{D}}$ the matrix equivalent of $\mathcal{D}$ and $\overline{\overline{\Gamma}}_{\text{xx}}$ the Gramian matrix of the pulse basis functions. The $N \times N$ complex capacitance matrix $\overline{\overline{C}} + \overline{\overline{G}}/j\omega$ can now be determined by exciting each conductor's ϕ_c with a unit potential in turn while keeping the others' equal to zero and integrating the resulting charges computed through (3).

The main difficulty remains with the construction of $\mathcal{D}$ or its discrete equivalent $\overline{\overline{D}}$, for which we adopt an approach similar to the one employed in [4], which constructs the (differential) DtN operator for the Helmholtz equation. Here, however, we require the DtN operator for the Laplace equation that governs the current capacitance problem.

Consider the arbitrary polygon illustrated in Fig. 2. On its boundary, which we define using the complex variable $\zeta = x + jy$, we invoke Green's second identity with the unknown ϕ and the known particular solution of the Laplace equation $\nabla^2_{xy} v = 0$, viz., $v = \exp(-j\lambda\zeta)$, to obtain the global relation [7]:

$$\oint_{\mathcal{C}} e^{-j\lambda\zeta}\left(\lambda\phi\,\mathrm{d}\zeta + \frac{\partial\phi}{\partial n}\,\mathrm{d}c\right) = 0. \tag{4}$$

Note that the other solution $\breve{v} = \exp\left(j\bar{\lambda}\bar{\zeta}\right)$, with $\bar{\cdot}$ the complex conjugate, results in an alternative, but equally valid global relation that also has to be considered to acquire the complete solution. Nevertheless, as the remainder of the procedure is completely analogous and for brevity, we will proceed with (4) only.

The first step in discretizing this continuous relation consists of the projection of the unknowns ϕ and $\partial_n\phi$ for each of the M sides of the polygon onto P Legendre polynomials $\mathcal{P}_p$:

$$\begin{Bmatrix} \phi_m \\ \partial_n\phi_m \end{Bmatrix} = \sum_{p=0}^{P-1} \begin{Bmatrix} C_p^m \\ D_p^m \end{Bmatrix} \mathcal{P}_p(t), \tag{5}$$

Substituting (5) into (4) yields, after some tedious calculations:

$$\sum_{m=0}^{M-1} e^{-j\lambda m_m}\frac{\sqrt{j2\pi\lambda h_m}}{\lambda h_m} \cdot \sum_{p=0}^{P-1} I_{p+1/2}(-j\lambda h_m)\left(\lambda h_m C_p^m + |h_m| D_p^m\right) = 0, \tag{6}$$

with $I_\nu(\cdot)$ the modified Bessel function of the first kind. By selecting Λ well-chosen spectral collocation points $\lambda \in \mathbb{C}$ [9]:

$$\lambda = -\frac{l}{h_m}, \qquad l \in \{1, 2, \ldots, \Lambda\}, \tag{7}$$

an overdetermined system is constructed out of (6) that can be solved for the coefficients C_p^m and D_p^m, resulting in the DtN matrix $\overline{\overline{D}}^*$. As a final step, this discretized operator in the Legendre domain is transformed to the sought-after matrix $\overline{\overline{D}}$ by means of analytically computed projection matrices between the polynomial basis and the local pulse functions.

III. Applications

We first consider a pair of coupled inverted embedded microstrip (IEM) lines with trapezoidal cross-section, shown in Fig. 3. The top ground plane and the two signal lines are made out of aluminum ($\sigma = 3.77{\cdot}10^7$ S/m) while the substrate supporting the lines is SiO_2 ($\epsilon_r = 3.9$, $\tan\delta = 0.001$), which in turn is bounded by a thick silicon slab with $\epsilon_r = 11.7$ and $\sigma = 10$ S/m resting on a PEC ground plane.

We now compute the 2×2 RLGC matrices and compare to a reference result [10], which uses a traditional DtN approach. Figure 4 shows the relevant elements of the $\overline{\overline{R}}$ and $\overline{\overline{L}}$ matrices while the unique entries of the $\overline{\overline{G}}$ and $\overline{\overline{C}}$ matrices are displayed in Fig. 5. All results show excellent agreement while the slight discrepancy in the inductance values between 10 MHz and 100 MHz can be attributed to the different approaches.

As a second example, we analyze a variation on the multiconductor transmission line (MTL) considered in [4] by

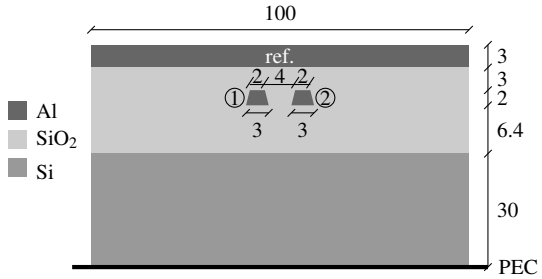

Figure 3. A pair of aluminum ($\sigma = 3.77 \cdot 10^7$ S/m) trapezoidal coupled IEM lines embedded in a silicon dioxide layer ($\epsilon_r = 3.9$, $\tan\delta = 0.001$), on top of a silicon substrate ($\epsilon_r = 11.7$, $\sigma = 10$ S/m), over an infinite PEC ground plane. All dimensions are given in µm.

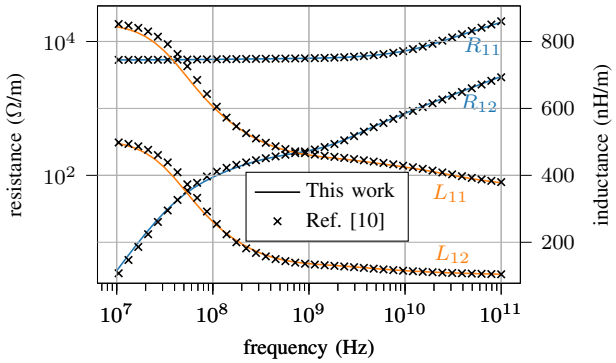

Figure 4. P.u.l. resistance and inductance matrix elements as a function of frequency for the IEM structure of Fig. 3.

introducing two additional lines and adding a lossy dielectric substrate ($\epsilon_r = 4$, $\tan\delta = 0.01$). The modified geometry, shown in Fig. 6, consists of five trapezoidal lines with a conductivity of $3.57 \cdot 10^7$ S/m. We investigate cross-talk for three different variations: the default isosceles trapezoid, an inverted trapezoid (bottom length: 0.75 µm; top length: 1.5 µm; height: 1 µm) and a rectangle with a width of 1.5 µm and height of 1 µm. The broadband RLGC parameters are calculated for these three configurations and promptly utilized to compute the scattering parameters of a 2 mm long transmission line. The near-end ports are numbered as indicated

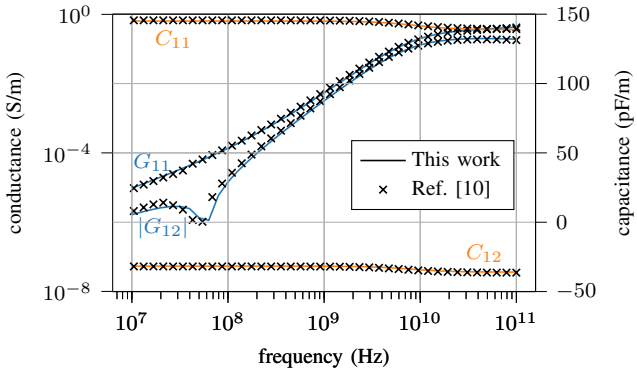

Figure 5. P.u.l. conductance and capacitance matrix elements as a function of frequency for the IEM structure of Fig. 3.

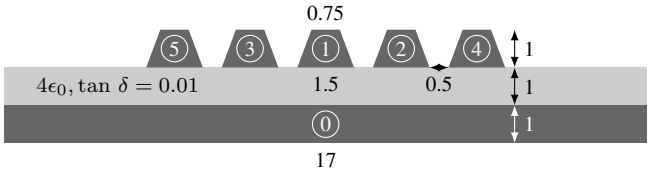

Figure 6. Multiconductor transmission line ($\sigma = 3.57 \cdot 10^7$ S/m) with five trapezoidal signal lines, a finite rectangular reference conductor and a lossy dielectric substrate ($\epsilon_r = 4, \tan\delta = 0.01$). All annotated dimensions are in µm.

in Fig. 6, with the corresponding far-end port bearing the near-end number plus five.

We consider line 1 to be the generator or aggressor line in this scenario and look at its S-parameters first in Fig. 7. The reflection coefficient S_{11} shows good matching along the entire broad frequency range. The trapezoid and its inverted version exhibit the same low-frequency value for this parameter due to them having the same resistance which changes around 10 GHz once the skin and proximity effect with the ground plane and the surrounding conductors start to play up. The DC resistance of the rectangular cross-section is, as expected, lower. The transmission of the primary line S_{61} shows similar behavior, viz., the two trapezoids express the same value until higher frequency effects in the conductors make the response split. Around the same point, the transmission starts to drop drastically regardless of the conductors' shape due to the skin effect and stronger coupling to the surrounding lines.

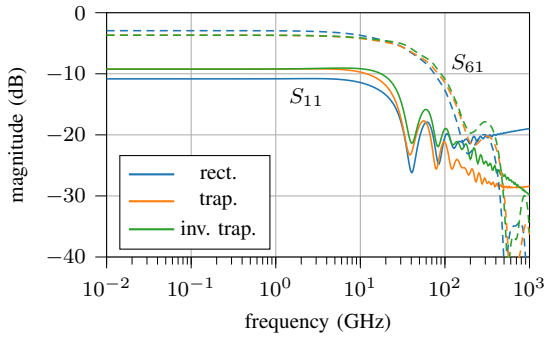

Figure 7. Reflection S_{11} (full) and transmission S_{61} (dashed) on the middle line of Fig. 6 for the three different conductor shapes.

In Fig. 8, we examine the near-end cross-talk, i.e., the signal picked up by *victim* lines 2 and 4 at the side of the generator. Some well-known results from established analysis of cross-talk on MTLs is clearly captured in these results. At the lowest frequencies the near-end cross-talk levels out due to common-impedance coupling as the return current in the ground plane experiences joule losses. Further on, the S-parameters increase rapidly once coupling between the lines picks up as predicted by the so-called inductive-capacitive coupling model. At the highest frequencies, wave effects, under the form of interplay between the several quasi-TM modes, are observed. The influence of the distance to the driving line is immediately clear by observing the difference

between S_{21} and S_{41} and the shape of the conductors influences the overall level of the near-end cross-talk.

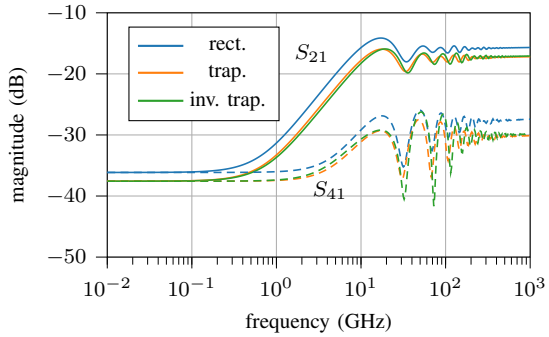

Figure 8. Near-end cross-talk on line 2 S_{21} (full) and line 4 S_{41} (dashed) with line 1 as generator for the MTL of Fig. 6 for three conductor shapes.

The effect of the agressor line on the same two victim lines is further characterized by S_{71} and S_{91}, respectively, as plotted in Fig. 9. This far-end cross-talk depends much more on the conductor's shape than any of the other examined quantities. The coupling to the closest line, i.e., line 2, in particular seems quite sensitive to the conductor's shape around 10 Gz, where the rectangular and trapezoidal cross-sections exhibit a sharp drop in the cross-talk which is barely present for the inverted trapezoid.

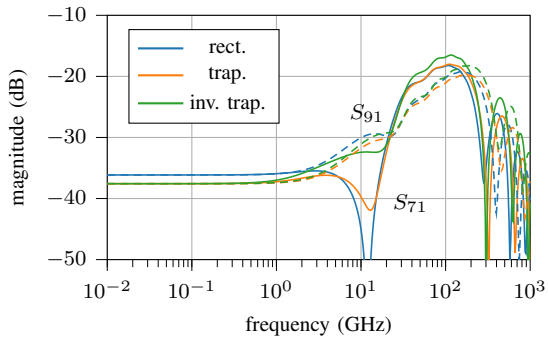

Figure 9. Far-end cross-talk on line 2, S_{71}, (full) and line 4, S_{91}, (dashed) with line 1 as generator for the MTL of Fig. 6 for three conductor shapes.

As a final example, we replace the non-magnetic metals in Fig. 6 by a material with a relative permeability of $\mu_r = 10$, preserving the electrical conductivity. Figure 10 contains a selection of the scattering parameters, viz., the reflection coefficient S_{11}, and near- and far-end cross talk on line 4, S_{41} and S_{91}, respectively, for the original conductor (shown in full lines) and the magnetic alternative (drawn with dashed lines). Some interesting phenomena stand out immediately. The S_{11} parameters exhibits a bulge around 10 GHz for magnetic conductors. This behavior shows remarkable resemblance to the difference between a single real pole and a complex pair in transfer function analysis, which can be attributed to the interplay of the capacitance and inductance of the line; the latter being much more prominent in the presence of the magnetic material. The other parameter that is heavily influenced by the magnetic contrast is the far-end cross-talk which is severely reduced.

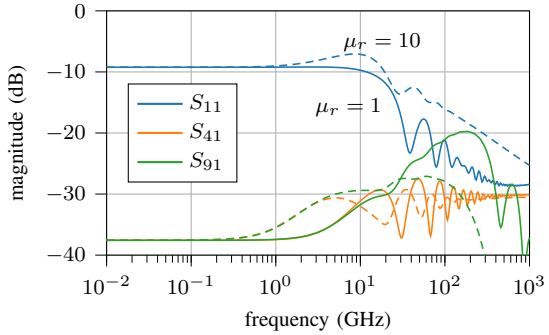

Figure 10. Reflection at primary line, S_{11}, near-end cross-talk on line 4, S_{41}, and far-end cross-talk on line 4, S_{91} for the trapezoidal MTL of Fig. 6 for non-magnetic metal (full) and magnetic conductors with $\mu_r = 10$ (dashed).

IV. Conclusion

This contribution presents a comprehensive modeling technique to compute the full RLGC per-unit-of-length parameters of interconnects with arbitrary polygonal cross-sections and generic, piecewise homogeneous materials through application of the numerically fast Fokas method. Consequently, the framework is applicable to the analysis of state-of-the-art interconnect structures, which exhibit intricate geometries due to design and manufacturing effects. The inclusion of magnetic materials in emerging interconnect design is also accomplished by the advocated method. The novel method is successfully applied to the analysis of cross-talk in a multi-conductor line with varying shapes and magnetic properties.

References

[1] J. Peeters, I. Bogaert, and D. De Zutter, "Calculation of MoM interaction integrals in highly conductive media," *IEEE Trans. Antennas Propag.*, vol. 60, no. 2, pp. 930–940, Feb 2012.

[2] T. B. A. Senior, and J. L. Volakis, "Approximate boundary conditions in electromagnetics," Institution of Electrical Engineers, 1995.

[3] D. De Zutter, and L. Knockaert, "Skin effect modeling based on a differential surface admittance operator," *IEEE Trans. Microw. Theory Techn.*, vol. 53, no. 8, pp. 2526–2538, Aug 2005.

[4] D. Bosman et al., "Interconnect Modeling using a Surface Admittance Operator Derived with the Fokas Method," *IEEE Conf. Electrical Perf. Electronic Pack. Syst. (EPEPS),* San Jose, CA, USA, Oct 2022.

[5] U. R. Patel, B. Gustavsen, and P. Triverio, "Proximity-Aware Calculation of Cable Series Impedance for Systems of Solid and Hollow Conductors," *IEEE Trans. Power Deliv.* vol. 29, no. 5, pp. 2101–2109, Oct 2014.

[6] T. Demeester, and D. De Zutter, "Construction of the Dirichlet to Neumann boundary operator for triangles and applications in the analysis of polygonal conductors," *IEEE Trans. Microw. Theory Techn.*, vol. 58, no. 1, pp. 116–127, Jan 2010.

[7] A. S. Fokas, "A unified transform method for solving linear and certain nonlinear PDEs," *Proc. R. Soc. A*, vol. 453, no. 1962, pp. 1411–1443, Jul 1997.

[8] T. Demeester, and D. De Zutter, "Quasi-TM transmission line parameters of coupled lossy lines based on the Dirichlet to Neumann boundary operator," *IEEE Trans. Microw. Theory Techn.*, vol. 56, no. 7, pp. 1649–1660, Jul 2008.

[9] M.J. Colbrook, N. Flyer, and B. Fornberg, "On the Fokas method for the solution of elliptic problems in both convex and non-convex polygonal domains," *J. Comput. Phys.*, vol. 374, pp. 996–1016, Dec 2018.

[10] D. Vande Ginste, and D. De Zutter, "Influence of the trapezoidal cross-section of single and coupled inverted embedded microstrip lines on signal integrity" *Proc. XXXth URSI GASS Sci. Symp.*, Aug 2011.